5-2021

Numerical Simulations of Density Waves in Saturn's A-Ring

Keaton Holt
Trinity University, holtkeaton@gmail.com

Numerical Simulations of Density Waves in Saturn's A-Ring

Keaton Holt

Abstract

In this work, we report on the use of a local cell N-body simulation method to model density waves in Saturn's A-ring. Specifically, we focus on waves excited at the 31-30 Inner Lindblad Resonance with Prometheus. We find that the local cell qualitatively matches larger cells in the formation process but is able to run more quickly and at higher resolution. The density waves that form in the local cell return theoretical surface density predictions (σ_0 = 46.51 g/cm^2) within 4% of the parameter value of 45.0 g/cm^2. Additional simulations run without particle self-gravity do not result in the formation of density waves, confirming that the waves are not a product of the cell or boundary conditions used. In the sudden absence of the moon, our simulations suggest that a fully formed density wave decays almost completely on the timescale of 1-2 years. However, a region of higher density appears to persist just outside the resonance location. Finally, by decreasing particle radius from 8.4m to 2.6m we were able to observe the formation of straw between wave peaks. Photometric renderings of these simulations show qualitative agreement with Cassini images.

Acknowledgments

I would like to thank Dr. Lewis and the Trinity University Physics and Computer Science Departments for advising me in preparing this thesis. This work was also supported by NASA CDAP Grant #80NSSC20K0480

Numerical Simulations of Density Waves in Saturn's A-Ring

Keaton Holt

A departmental senior thesis submitted to the
Physics Department at Trinity University in
partial fulfillment of the requirements for graduation
with departmental honors.

April 23, 2021

Thesis Advisor

Department Chair

Associate Vice President
for
Academic Affairs

Numerical Simulations of Density Waves in Saturn's A-Ring

Keaton Holt

Contents

Chapter 1

Introduction

Density waves are one of the more visible features of Saturn's A-ring. The analytic theory behind these structures has been well understood for years [16], but they haven't been explored with N-body simulations. This is in part due to the assumption that these simulations would need to be global to capture the dynamics of density waves, and such simulations require a large number of particles in order to achieve reasonable resolution. In this work, we aim to show that local simulation cells can reproduce density waves without the need for excessively long running time.

After establishing the validity of the local cell method, we extend our analysis in two directions. First, large perturbations to the resonant forcing can be observed in multiple locations in Saturn's rings. For example, density waves created by the Janus-Epimetheus horseshoe orbit [14] are locked into a building and damping cycle due to periodic swaps of the moons' orbits. We look to our local cell simulations to approximate the damping process when the moon's gravity is suddenly removed. Second, density wave observation has shown that fine-grained structure called straw often forms between wave peaks [13][7][19]. By enhancing the resolution of our local cell, we seek to examine such structure in our simulations.

Chapter 2

Background

Density waves are structures which owe their formation to resonances between ring material and one or more perturbing bodies. They are characterized by a decaying amplitude and wavelength over 10km length scales. Here we cover the relevant physics to describe density waves in Saturn's A-Ring as well as the computational methods used to build and simulate the system.

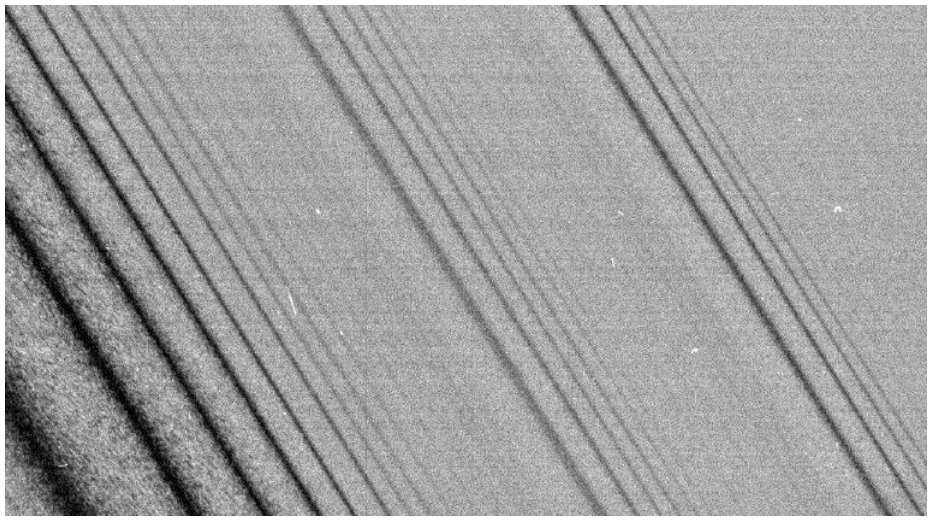

Figure 2.1: A Cassini image of the Janus 6:5, Janus 4:3, and Prometheus 33:32 density waves (left to right). Figure from Figure 5H of [11].

2.1 Density Waves History

Density waves, first proposed by Julian and Toomre in 1966 [4] for disk galaxies, have been studied extensively by theoretical and experimental physicists alike since the 1980s. The Voyager missions' visits to Saturn in 1980 and 1981, followed by Cassini's 2004-2017 period of observation, provided ample evidence and example of density waves in Saturn's rings (Figure 2.1).

2.2 Resonances in Saturn's Rings

For ring particles orbiting a planet under the influence of an external moon, we view the system through the lens of a rotating reference frame in which the moon is stationary. In this frame, the ring particles orbit the planet, experiencing a gravitational "tug" from the moon each time they pass by. A particle and moon pair which satisfy the condition for an Inner Lindblad Resonance (ILR) have a similar relationship to a simple harmonic oscillator. Each time the particle completes m orbits, the moon has completed exactly $m-1$ orbits, such that the masses are aligned. At each such conjunction, the particle is pulled into a more eccentric orbit. For a nearly spherical planet, each particle's epicyclic (radial) frequency κ and mean motion (orbital frequency) n are equal, causing successive kicks to interfere constructively. This gives rise to an increasingly well-defined wakelike structure at the resonance location. The condition for a strong Inner Lindblad Resonance (ILR) is as follows:

$$m(n - \Omega_M) = \kappa \tag{2.1}$$

where Ω_M is the mean motion of the reference frame about the planet, n is the mean motion of the particle, κ is the epicyclic frequency of the particle's orbit about its guiding center, and m is an integer [11]. When the planet is nearly spherical, we let $\kappa \to n$ so that the above condition can be rewritten to define the necessary orbital period for a particle to

enter a resonance as a function of the orbital period of the moon:

$$T_P = T_M \left(\frac{m}{m-1} \right) \tag{2.2}$$

Because the orbital period, T_P, of the particle depends on its separation distance from the planet, many ILR's are possible for a given moon. Resonances are classified by their resonance number as $m : m-1$ (see Figure 2.1).

2.3 Formation of Density Waves

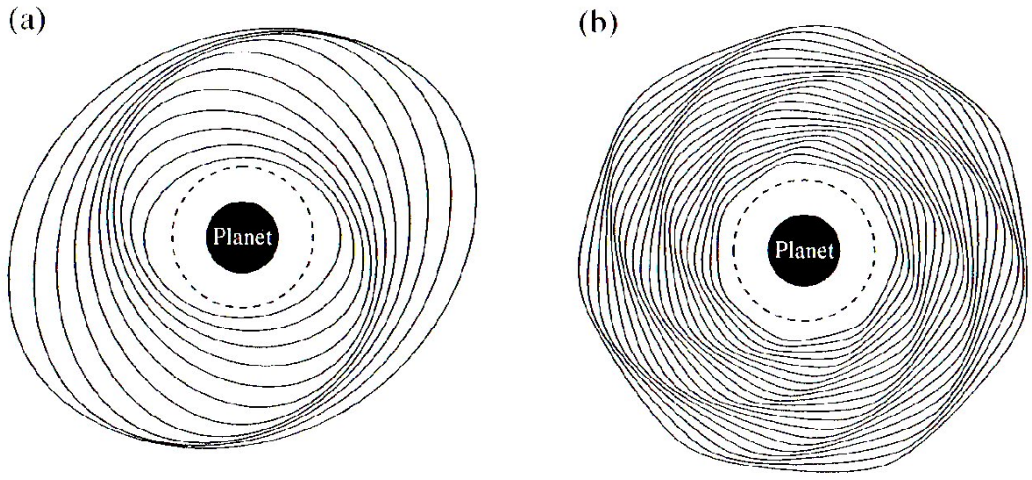

Figure 2.2: Schematic diagrams of the coplanar particle paths that give rise to trailing spiral density waves near a resonance with an exterior satellite. (a) The two-armed spiral density wave associated with the 2:1 (m=2) inner Lindblad resonance. (b) The seven-armed spiral density wave associated with the 7:6 (m=7) inner Lindblad resonances. The pattern rotates with the angular velocity of the satellite and propagates outward from the exact resonance (denoted by the dashed circle). Figure and caption from Figure 10.11 of [11].

Figure 2.2 demonstrates the beginning stages of the formation of a density wave. Particles nearest to the exact resonance location are pulled into orbits of increasing eccentricity, while those slightly off resonance do not receive as strong of a kick. The result is a wake

structure in which regions of ring material are alternately compressed and rarefied. As these high-density areas are formed, their collective self-gravity reinforces and "communicates the disturbance" away from resonance. Viscous damping (particle collisions) causes the wave to lose both amplitude and wavelength in a predictable manner that can be used to estimate the density of the ring material [16].

2.4 Guiding-Center Coordinates

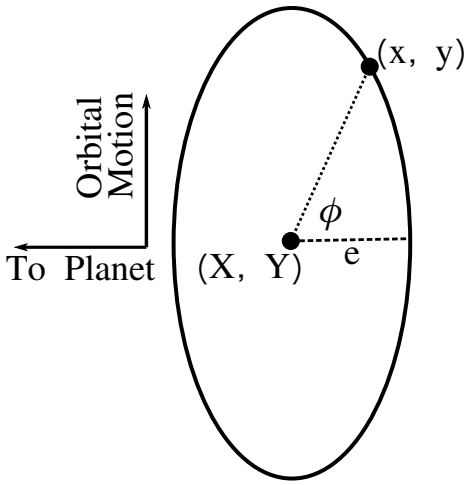

Figure 2.3: Schematic for the GC coordinate system (created by Mark Lewis).

For very-nearly circular orbits (eccentricity $e << 1$) particle motion can be approximated to first order in e through the use of a Guiding-Center coordinate (GC) system. This method views the global movement of particles as elliptical motion about a "Guiding Center" point which follows a circular trajectory around the planet. Our simulations assume a spherical Saturn with all ring particles as well as the moon in a single plane, so the GC system should derive from the natural choice: a cylindrical coordinate system (r, θ, z). Our simulations examine a local region in r near the resonance location r_0, so we can introduce a local cartesian system in which $x = r - r_0$, $y = r_0(\theta - \Omega_M t)$, and z is

unchanged. Finally, these coordinates can be transformed to a GC system $(X, Y, e, i, \phi, \zeta)$ via the following relationships:

$$\begin{aligned} x/r_0 &= X - ecos\phi \\ y/r_0 &= Y + \beta esin\phi \\ z/r_0 &= icos\zeta \\ \phi(t) &= \kappa t + \phi_0 \\ \zeta(t) &= \mu t + \zeta_0 \\ Y(t) &= -2A_0 X t + Y_0 \end{aligned} \tag{2.3}$$

where e is the eccentricity, i is the inclination, ϕ is the epicyclic phase angle, and ζ is the phase of inclination. Finally, the new X, Y represent the position of the particle's guiding center, meaning X is constant (circular motion). The benefit of this approximation and transformation is that particle motion due to the gravity of the planet is now defined analytically in terms of the time t. Perturbations caused by the moon's gravity, collisions and particle self-gravity must be factored in separately. See [8], [6], and [18] for more on these transformations.

2.5 Collisions

Collisions between particles are handled using a smooth, hard-sphere method in which initial and final velocities are related by a speed-dependent coefficient of restitution ϵ [1]:

$$\epsilon(v_\perp) = min(0.34 v_\perp^{-0.234}, 1) \tag{2.4}$$

This means that faster-moving particles will have their velocities reduced by a greater fraction than slower-moving particles and introduces an overall damping of kinetic energy.

For each small timestep dt, we use a spatial hash to search for all collisions with nearby particles that will occur during that step. Collision pairs are then handled sequentially by assuming linear motion through dt [8][1].

2.6 Simulations and Boundary Conditions

We replicate the dynamics of particles near the 31-30 resonance with Prometheus in the A-ring using N-body simulations [10]. Each particle stores its 3-dimensional position, 3-dimensional velocity, and size, which are updated at each time step as they interact via gravity and collisions. We rely on the Guiding Center approach to approximate the orbital motion of the particles in the rest frame of the perturbing moon and use a hard-sphere model to determine the outcome of collisions between particles. We use a KD tree to calculate particle self-gravity. The 3 boundary conditions used in our simulations are described below and by Figure 2.4.

1. Global Cell

   This boundary condition applies to a band of particles spanning the entire azimuthal extent of the ring. In the simulation, the band is represented as a rectangle centered radially on the resonance location such that particles exiting on one edge of the cell are wrapped back into the other.

2. Single-Orbit Cell

   This boundary condition applies to a group of particles whose azimuthal bounds are chosen such that the azimuthal extent is equal to the particle drift relative to the moon in one orbital period. This choice produces a cell in which particles at the leading and trailing ends receive the same resonant "kick" from the moon when they pass. Because particle drift rate depends on the radial coordinate, the cell is not a perfect rectangle but instead is slightly tapered and trapezoidal. This condition requires the

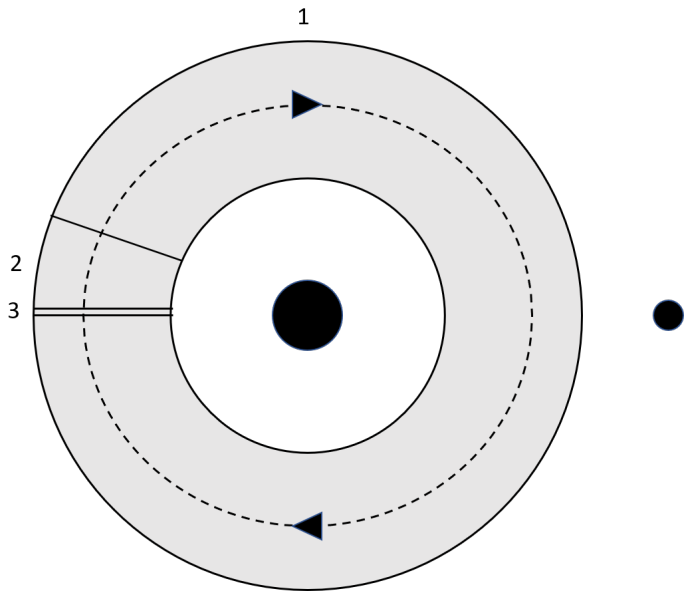

Figure 2.4: The three boundary conditions used in our simulations as shown in the rotating reference frame of the stationary moon. 1) global cell 2) single-orbit cell 3) local cell

cell to span $2\pi/m$ radians where m is the resonance number.

3. Local Cell

   This boundary condition uses a group of particles spanning a small azimuthal length. The azimuthal scale is similar to the radial scale for these simulations. The local cell uses periodic boundary conditions to wrap exiting particles back into the cell, however, the epicyclic phase of those particles are offset by an amount equal to the epicyclic motion that occurs for a particle drifting from one azimuthal edge to the other. See Lewis and Stewart's (2002) Equation 6 and accompanying text for further discussion of this boundary condition [6].

Table 2.1 contains the parameters for each of the three simulation types described above. While selection of radial cell size and particle radius is technically arbitrary, we require all simulations to conform to a surface mass density (45 g/cm^2) and single-particle densities

(0.4-0.5 g/cm^3) based on observations [17][12]. These choices and physical requirements, combined with the azimuthal cell size defined by the boundary condition, determine the number of particles the simulation must include. Because the area of the global cell is larger than that of the local cell by nearly a factor of 10^5, for example, global simulations need roughly 10^5 times as many particles as compared to a local simulation with equal particle size.

Boundary Condition:	Global	Single-Orbit	Local
Particle Radius (m)	140	56	8.4
Single-Particle Density (g/cm3)	0.4	0.4	0.5
Particle Count (millions)	3.5	2.6	1.3
Azimuthal Cell Size (radians)	2π	0.2	0.00004
Radial Cell Size (km)	40	60	60

Table 2.1: Parameters for each boundary condition. All simulations use a surface mass density of 45 g/cm^2.

Chapter 3

Validating the Local Cell Method

3.1 How Useful is the Local Cell?

As demonstrated by Table 2.1 of the previous chapter, global simulations tend to require larger particles, more of them, and a smaller radial cell width. These undesirable parameters result in excessively long running times and limited resolution, making it nearly impossible to uncover the fine structure of density waves. Seeking to legitimize the use of a local cell for density wave simulations, we show that the local simulation method described in Chapter 2 is consistent with global simulations and density wave theory. We also compare our results to simulations omitting particle self-gravity to demonstrate that the waves that form are not an artifact of the choice of cell size or boundary conditions.

3.2 Methods

To validate our local cell method for producing density waves, we ran and compared the outputs of 4 unique simulations. First, global, single-orbit, and local cell simulations were run and compared at the farthest step of the global simulation. A second comparison was made between the single-orbit and local cells at the farthest step of the single-orbit

simulation. Finally, a fourth local cell simulation with 1.5x the radial extent of the cell described by Table 2.1 and a correspondingly larger number of particles ($\sim$ 2.9 million) was left to run to 2000 orbits. This cell would be used for analysis following comparison of the other three simulations.

3.3 Comparison of Boundary Conditions

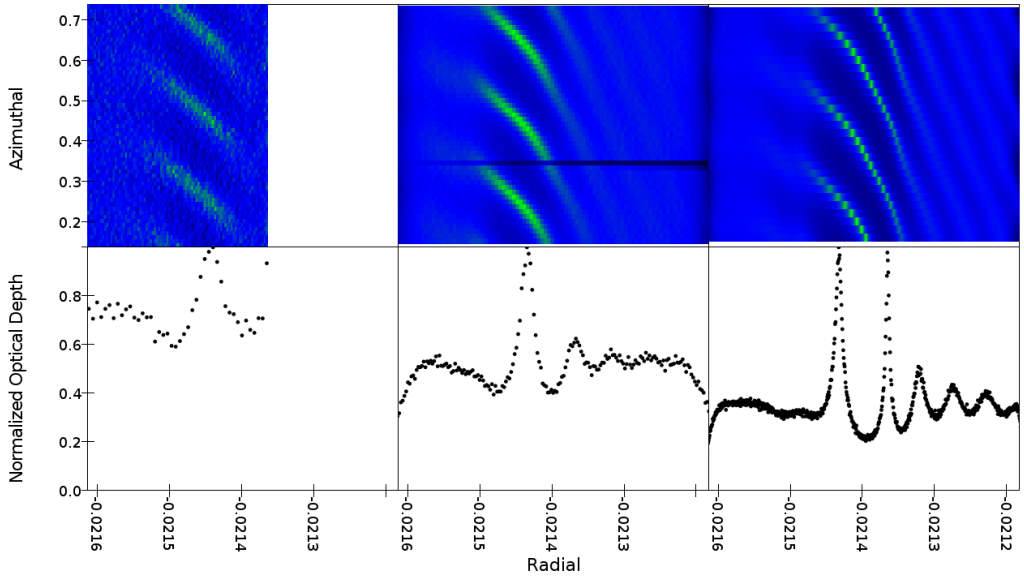

Figure 3.1: A comparison of the 3 boundary conditions after 427 orbits. From left to right: global, single-orbit, and local. In the top row, green indicates high optical depth while dark blue indicates low optical depth. The y-axis marks the azimuthal coordinate. The bottom row is a horizontal slice across the center of the cell with the y-axis representing optical depth. Both plot types use a radial coordinate in units of the orbital radius of Prometheus, which sits at r = 0.

The 3-panel Figure 3.1 indicates the formation of a density wave across all 3 simulations. In particular, the single-orbit and local cell slices (bottom row center-right) possess a decreasing wavelength, a decaying amplitude, and propagation of the wave away from the resonance location, the key characteristics we look for when identifying a density wave.

The global cell's smaller radial extent makes it harder to identify such features, but we take the qualitative similarity of all 3 simulations as evidence that the structure formed is not a byproduct of the boundary conditions used.

The 2-panel Figure 3.2 shows continued agreement between the boundary conditions. While the global simulation was too computationally demanding to reach this point, we look to the continued structural similarity of the remaining two simulations as reason to trust the local cell when analyzing the characteristic decay in wavelength of the density wave. Differences can be attributed largely to the particle sizes involved in each simulation, as smaller particles in the local simulation allow for sharper peaks in the optical depth. Note also that the use of binned data for the local cell plots introduces "pixelation" in the upper right panel when compared to the upper left. This is because we must bin and average the optical depths of the local cell for each of the 31 steps it takes for the cell to drift an azimuthal distance equal to that spanned by one step of the single-orbit cell.

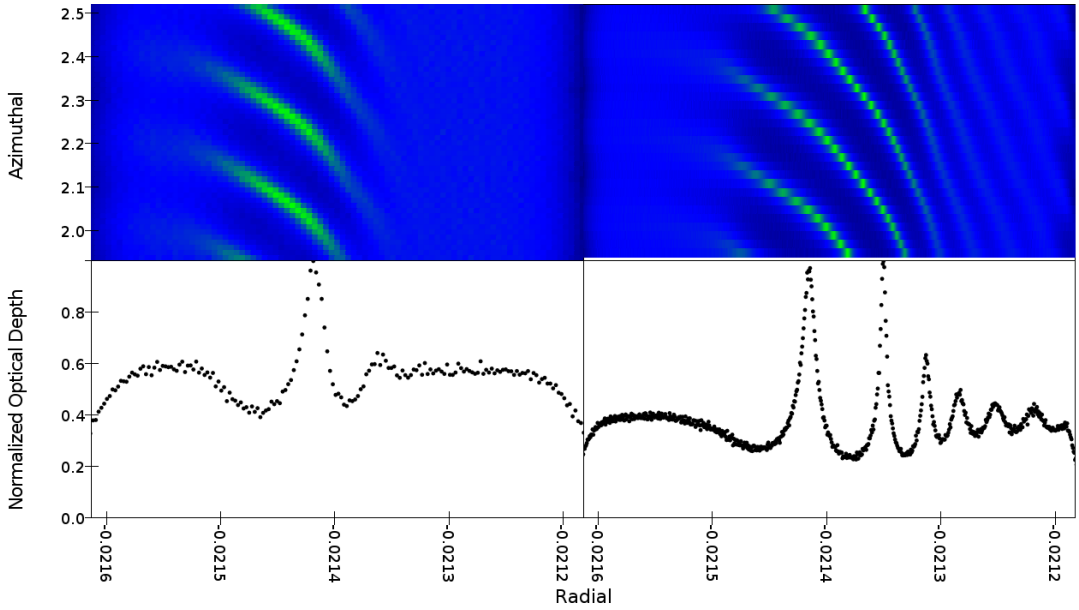

Figure 3.2: A comparison of the output of the single-orbit (left) and local (right) simulations after 594 orbits. The axes and heat maps represent the same quantities as in Figure 3.1.

3.4 Density Wave Analysis

Taking Figures 3.1 and 3.2 as evidence of the legitimacy of the local cell method, we turned to the larger local cell to analyze the density wave. The larger cell allows us to ensure that the wave train has fully damped out by the time it reaches the edge of the cell, and thus that no boundary effects are contributing to the structure. Figure 3.3 shows an example output from a single step of the simulation. At each step, we partition the particles across the cell (radially) into 1000 bins, calculating the average optical depth in each. Each black point in the plot at left reflects this relationship, with optical depth plotted as a function of the radial coordinate.

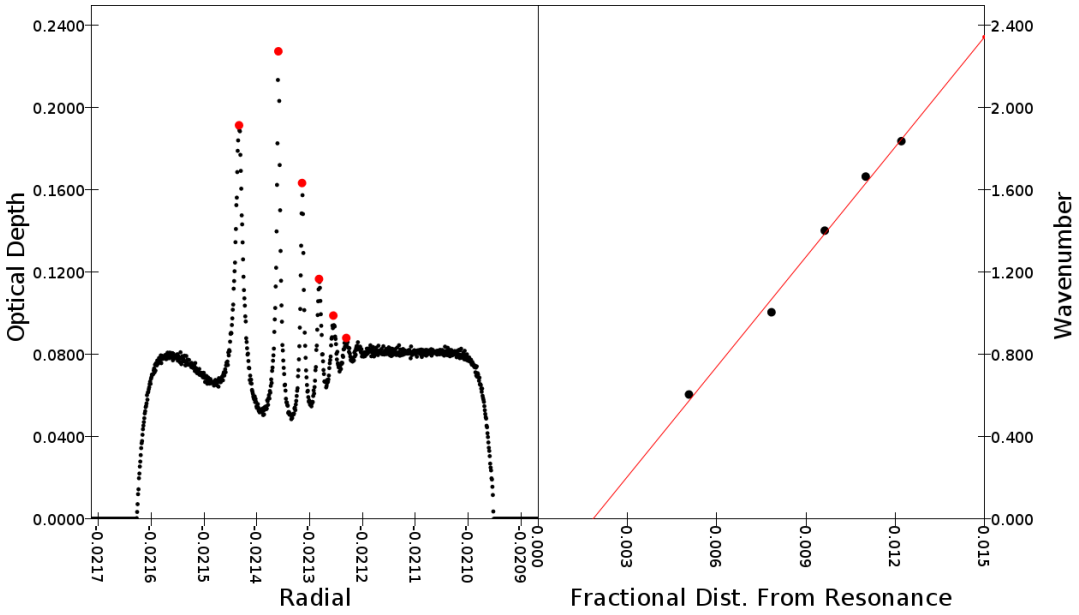

Figure 3.3: At left: the optical depth plotted as a function of the radial coordinate (units of Prometheus' orbital radius), where red dots mark the position of wave peaks. At right: the separation between these peaks (the wavelength) is calculated and then inverted to give the wavenumber k over each interval. The wavenumber (units of km^{-1}) is plotted as a function of the wave's average fractional distance from resonance during that interval. See https://youtu.be/GwMAbc0CwN4 for a movie version of this plot containing slices across many simulation steps.

Theory predicts the wavenumber k according to Equation 3.1 [5]:

$$k(x) = \frac{3(m-1)\Omega_L^2}{2\pi G\sigma_0}x \tag{3.1}$$

where x is the fractional distance from resonance, m is the resonance number (31 in our case) and Ω_L is the orbital frequency of the resonance location. σ_0 is the surface density, which we use as a parameter for our simulations and therefore expect to match this equation for fully-formed density waves. To verify that the relationship holds, we implemented a peak-finding algorithm to calculate wavelengths and wavenumbers by locating maxima. Though we experimented with a number of techniques based on parabola-fitting, we ultimately decided to simply select local maxima based on a minimum radial spacing and optical depth. Red dots indicate points taken to be maxima by the algorithm. Next, radial separations between adjacent peaks, or wavelengths, were calculated and inverted to give the wavenumber. The plot at right of Figure 3.3 contains the wavenumber k plotted as a function of the average x-value for each peak separation within this snapshot of the wave. Since Equation 3.1 is linear in x, we found the slope of these data (red line) and rearranged the equation to give the surface density σ_0 as a function of the slope k/x:

$$\sigma_0 = \frac{3(m-1)}{2\pi G(\frac{m-1}{m}T_{moon})^2} * \frac{1}{\text{slope}} \tag{3.2}$$

where we replace the orbital frequency of the resonance location with T_{moon} the orbital period of Prometheus, for ease of calculation. By compiling the wavenumbers and corresponding x-values for a wide range of snapshots (10 per orbit over more than 500 orbits) and plotting them together, we arrived at Figure 3.4.

Apparent "quantization" at the upper limit of Figure 3.4 is due to the practical limits of binned data. Because we calculate optical depths for 1000 evenly-spaced radial locations across the cell, we inevitably run into problems in this plot as large wavenumbers (small

wavelengths) run up against the finite spacing between binned data points. We are unsure as to the reason for curvature at the lower limit, though high-density nonlinear effects, inner boundary effects, and too-large particles are potential culprits. Though the combined data do not fit as nicely to the linear model as in the individual snapshots, we can still apply Equation 3.2 to the slope of Figure 3.4 (red line, slope = 175.753km^{-1}) to get a working estimate. Plugging in other known constant values, we arrive at a calculated σ_0 = 46.51g/cm^2. This value is within 4% of our parameter value of 45 g/cm^2, in good agreement with theory.

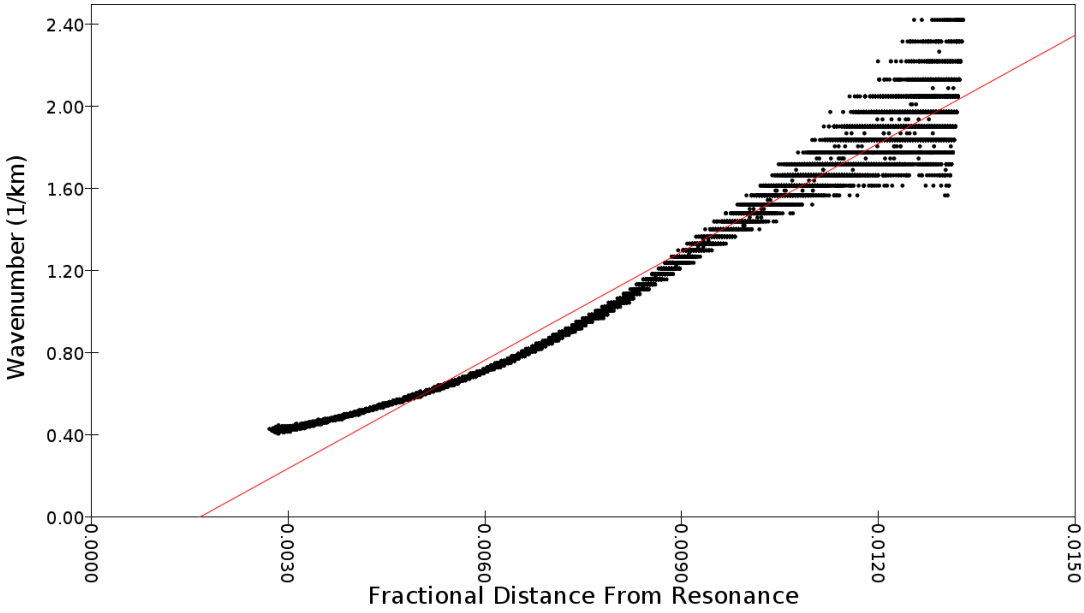

Figure 3.4: A compiled plot of wavenumbers from the extended local cell simulation, again as a function of the fractional distance from resonance. The simulation's first 1000 orbits are not considered so as to focus on fully formed density structures and allow transient effects to die out.

3.5 Simulations without Self-Gravity

As a final demonstration of the validity of the local cell, we ran each of the 3 simulations compared in Figure 3.1 again. This time, however, we omitted particle self-gravity such that all motion was determined by Equations 2.3, the moon's gravity, and collisions. Figure 3.5 contains the results. No density wave structures form, only wake peaks at the resonance location due to repeated encounters with the perturbing moon, Prometheus. While a small wavelike structure appears to form in the local cell simulation, it does not possess the characteristic decrease in wavelength that we associate with a density wave. The lack of density wave formation in these simulations means that the density waves observed in our other simulations must be the result of particle self-gravity. They are not a product of the choice of cell size or boundary conditions.

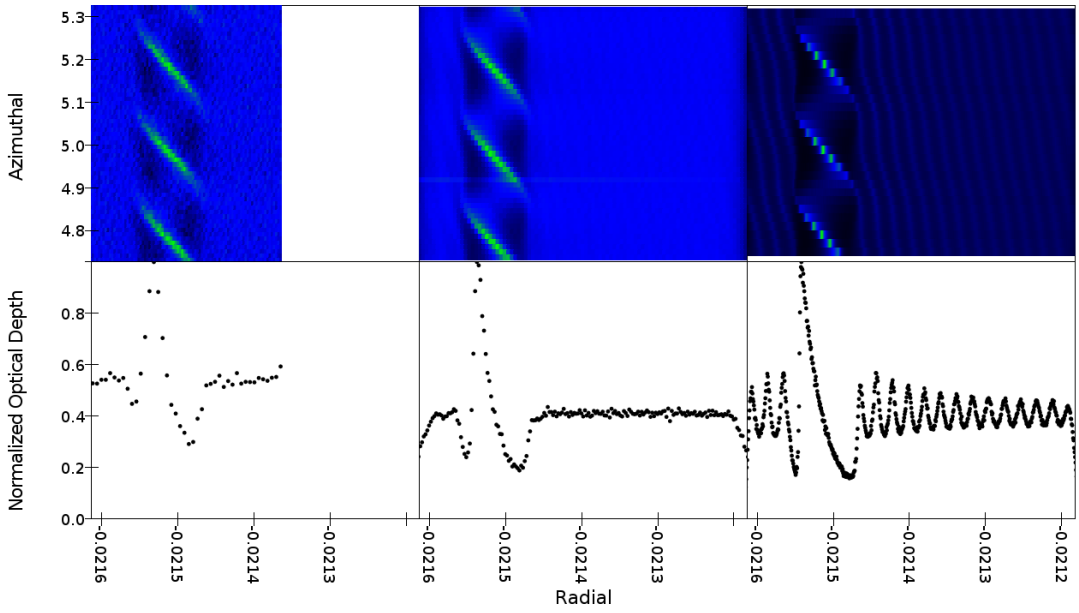

Figure 3.5: All 3 simulations were re-run without particle self-gravity (shown here at 986 orbits). The axes and heat maps display the same quantities as Figures 3.1 and 3.2.

Chapter 4

Varying the Perturbation

4.1 Temporal Variations

Typical simulations begin with a random, featureless distribution of particles which is then slowly shaped by the perturbing moon until we see wake structures (see Figure 3.1) and then density waves. After approximately 1000 orbits, the local cell simulations tend to reach a steady state where the eccentricity and optical depth are unaffected by further passes by the moon. Though most real density waves in Saturn's rings exist only in this steady state, there are a few examples for which this is not the case. The horseshoe orbits of Janus and Epimetheus (two of Saturn's moons) give rise to numerous density waves at resonance locations in the A and B rings. However, as demonstrated by Figure 4.1 , the moons "swap" orbital radii every 4 years, changing the resonance locations. This poses an interesting system for analysis because the density waves formed at those locations must form and dissipate periodically. In their analysis of observational data obtained from the Cassini mission, Rehnberg et. al. [14] find that the old density wave tends to dissipate on the timescale of one year while a "solitary wave" is launched outward from the old resonance location. With this paper in mind, we decided to run a simulation beginning

with a steady-state density wave configuration in which the moon perturbation was "turned off". In addition to studying this system, a talk by Matt Hedman [3] at the 2020 Division

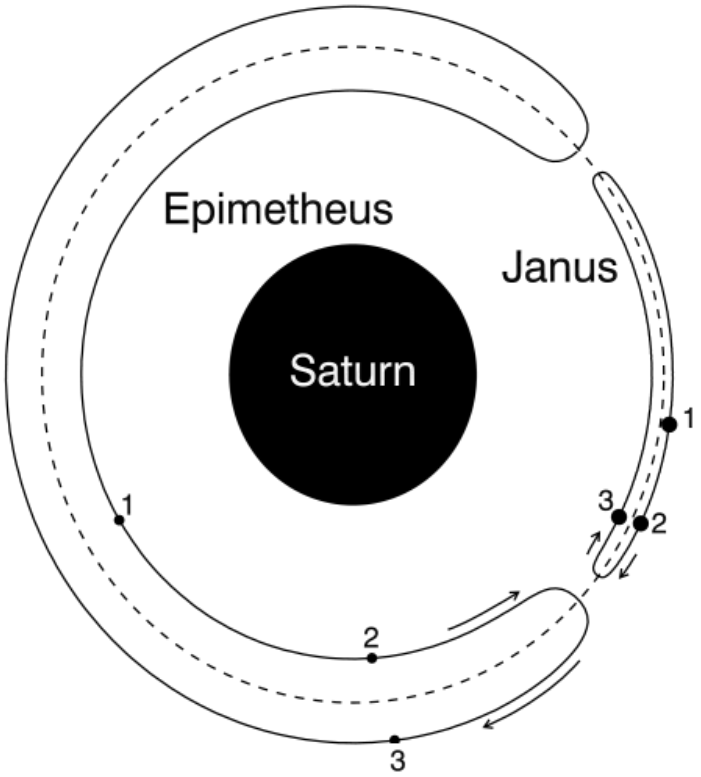

Figure 4.1: A drawing of the horseshoe orbits of Janus and Epimetheus. Figure from: https://www.groundai.com/project/the-rotation-of-janus-and-epimetheus/2

for Planetary Sciences of the American Astronomical Society Conference gave us another reason to consider running a simulation with a modified moon perturbation. Saturn's C ring contains numerous examples of density waves which form, dissipate, and reform over time due to asymmetries in Saturn's gravitational field. Because analytic models cannot handle such large changes to the perturbing force, simulations are the best strategy for exploring these types of systems.

4.2 Methods

As an initial attempt to model a suddenly-disappearing moon perturbation, we used as initial conditions the final step in the local cell simulation described by Table 2.1. Though we saw a slight outward (toward the satellite) density migration, we saw little damping of the existing density wave before boundary effects started to become a concern. The relatively small radial extent of our cell meant that as slight damping and outward migration did occur, waves carrying these particles were partially reflected at the boundary, introducing non-physical energy and angular momentum back into the cell.

To remedy the problem of boundary interference, we used as initial conditions the final step of the radially larger local cell simulation described in Chapter 3. This simulation would hopefully contain sufficient material to damp outward-bound particle migrations before they reached the boundary. Though we still see boundary interference, the effect is less pronounced.

4.3 Results

Figures 4.2, 4.3, and 4.4 visualize the damping of the density wave over the course of approximately 1000 orbits (1-2 years of real time) when the perturbing moon is suddenly removed. In the (top) eccentricity plots of Figures 4.2 and 4.3, we can see that the high-eccentricity region (red) shifts radially outward while decreasing in magnitude. This continues until we reach a background state (dark-purple) of evenly distributed eccentricities. In the (middle) optical depth plot of Figure 4.2, we also see a slight outward shift and significant damping of the densest (purple) regions, though we do not reach a uniform state. Instead, formation of the density wave creates a relatively permanent region of higher density extending outward from the resonance location.

The optical depth plots of Figure 4.3 give us further insight into the damping of the

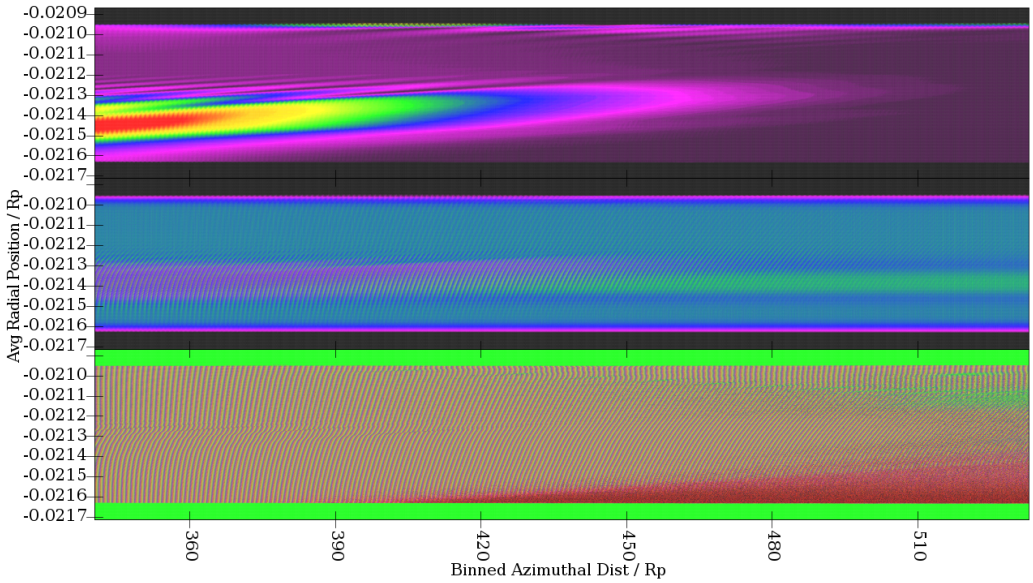

Figure 4.2: Damping of the Density Wave. From top to bottom: eccentricity, optical depth, and epicyclic phase as functions of the azimuthal coordinate of the cell and radial coordinate across the cell. The resonance location is $r = -0.0215R_p$

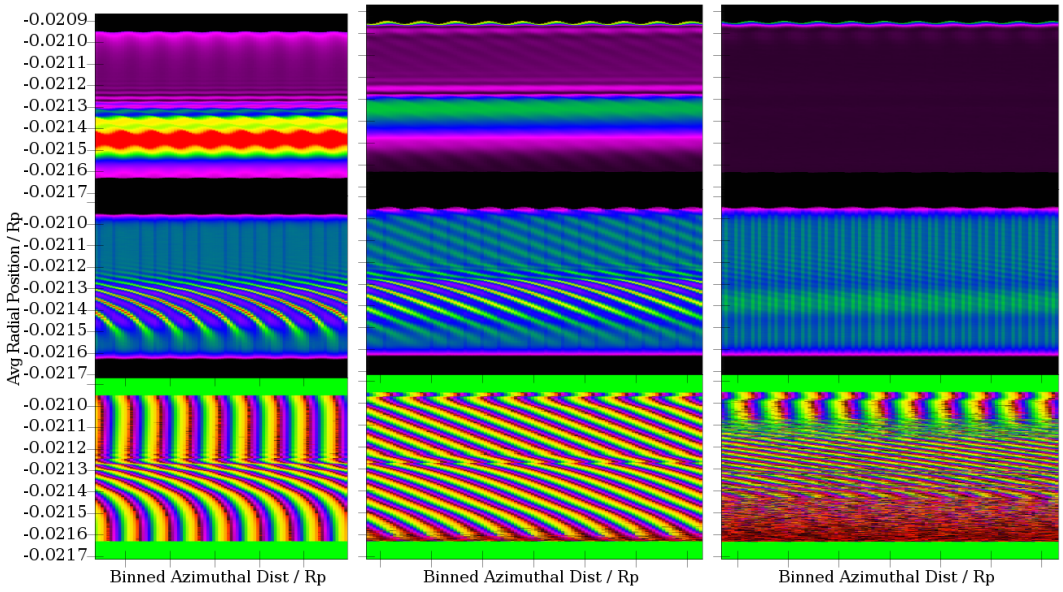

Figure 4.3: Zoom-ins of Figure 4.2 at 340-342 radians, 410-412 radians, and 530-532 radians.

density wave through the cant angle. In the left plot, high-density regions bend at two angles. Closer to resonance, the cant is near-vertical, indicative of a still-dominant density wave. Further from resonance, the cant trends toward horizontal due to resonant moon-wake effects which form independent of particle self-gravity. As we move to the second (center) plot, the cant angles have shifted away from vertical, demonstrating the decreasing relevance of the density wave. By the time we reach the right plot, neither moon-wakes nor the density wave remain.

The final rows of Figures 4.2 and 4.3 plot the epicyclic phase angle ϕ, and confirm the analysis of the preceeding paragraph. Again, we see the cant angle shift from density wave-dominated to moon wake-dominated to a nearly random distribution. This process is essentially the reverse of what we see in the formation of a density wave from an initially random distribution of particles.

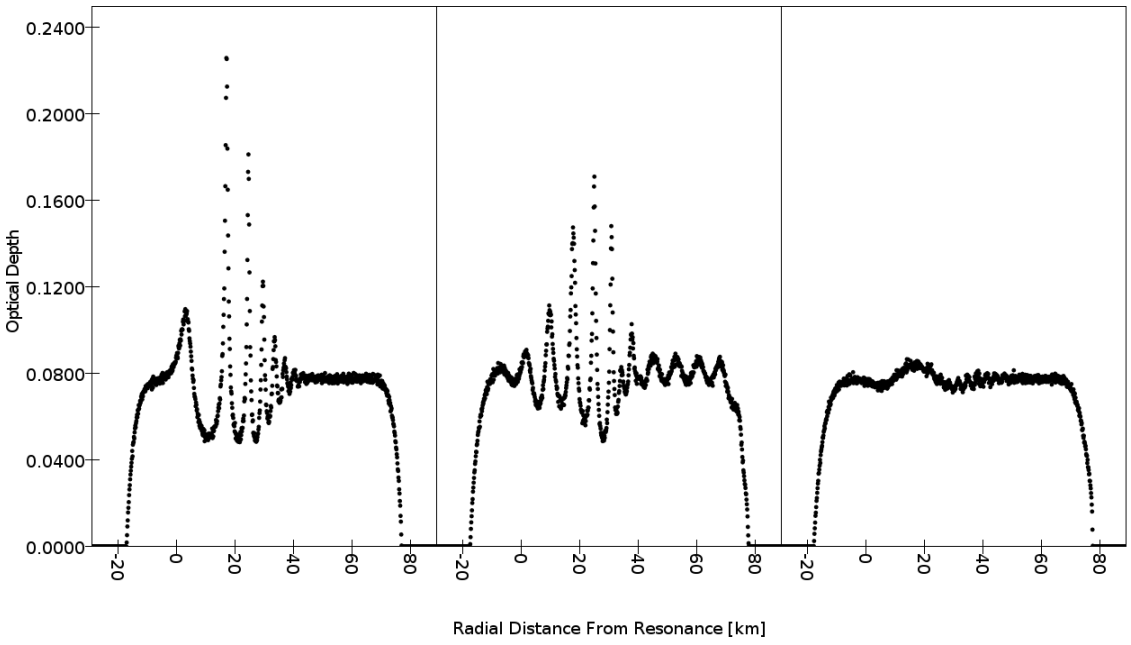

Figure 4.4: Slices across the (azimuthal) center of the cell after 1 orbit, 400 orbits, and 975 orbits following removal of the moon. Optical depth is plotted as a function of the distance from the radial resonance location.

Finally, Figure 4.4 gives another look at the optical depth profile of the cell at three locations in time. Each plot bins the particles across the azimuthal center of cell, calculating the average optical depth as a function of the distance from resonance (related to the radial coordinate used above by a simple linear transformation). Just as in Figure 3.3, decreasing amplitude and wavelength with increasing distance from resonance clearly indicate a healthy density wave. As we step forward in time without the moon, however, the wave cannot sustain itself and begins to crash (middle plot) before flattening out (right plot). As noted previously, the density wave does leave behind a region of high-density particles extending outward $\sim$20km from resonance.

Chapter 5

Improving Resolution

5.1 Computational Limitations

The resolution of our simulations is currently limited by the size of our simulated particles, which tend to be "larger than life" in order to restrict the total number of particles. In addition to improving resolution, smaller particles better represent the actual size distribution of ring particles, which are estimated to range from cm-scale to ∼5m in radius [2]. In order to conserve total mass while maintaining the same particle density, however, we need to dramatically increase the number of particles N for small changes in particle size r:

$$M_{tot} = Nm = N\left(\frac{4}{3}\pi r^3 \rho\right) \longrightarrow Nr^3 = \text{Constant}$$

With particle counts already exceeding 1 million in the local simulation method (Table 2.1), this conservation of mass requirement unfortunately means higher-resolution simulations will run significantly slower. In fact, we reach the limit of our machine's memory usage above about 40 million particles, so the particle radius cannot be cut to less than $(N/N')^{1/3} \approx (1/40)^{1/3} \approx 0.29$ of its original value.

5.2 Straw

Observations from the Cassini mission show a number of places in the A-ring where clumpy features called "straw" are present [13][7][19]. Figure 5.1 shows the presence of straw in the troughs of the three density waves pictured. The mechanism by which these structures

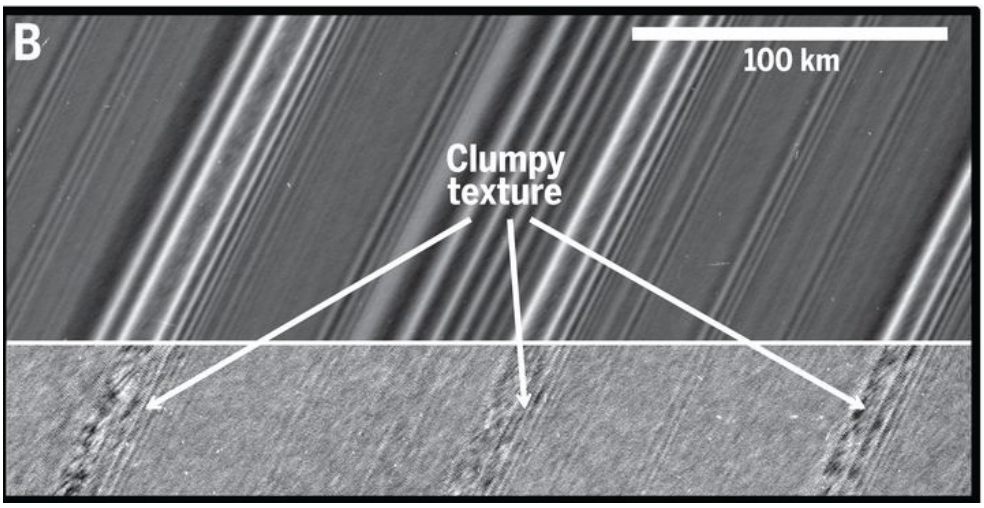

Figure 5.1: Straw in the troughs of the Prometheus 26:25, 27:26, and 28:27 density waves (left to right) in the outer A ring. Caption and figure from Figure 2B of [19].

form is not well understood, though the process may be spurred along by self-gravitation as nearby particles pull and clump together into gravitational "wakes" [9]. As these wakes form, tidal forces cause resulting clumps of particles to shear out, as particles nearer to the planet move more quickly than those more radially distant. This produces "stringy" features qualitatively similar to those we see in Figure 5.1. Whereas straw can be seen at length scales of 1km, however, normal gravitational wakes tend to have lengths on the order of 100m or smaller, depending on surface mass density. We hypothesize that the structure and collective motion of density waves may allow extended wakes to form. By improving the resolution of our simulations, we aim to discover whether we have captured the physics which produce this clumping in and around regions in which density waves are present.

5.3 Methods

As discussed above, the running time for a simulation with millions of particles rapidly increases with particle count. It would be hopeless, for example, to start a simulation with a random distribution of 40 million particles and wait for density waves to form. Instead, we planned to replace the existing particles from the final step of our usual local cell simulation with a new, larger set of particles matching the properties of the original. A new, higher resolution simulation would begin with this larger, redistributed set of particles as its initial conditions. The redistribution process is non-trivial, however, as replacing each single spherical particle with multiple smaller spheres necessitates that the new spheres occupy a larger volume. This could potentially cause overlap issues with neighboring particles, so we opted for a different strategy. First, we divide the existing particle distribution into a grid in guiding-center coordinates, calculating the mean and standard deviation of each of the 6 orbital elements (see Section 2.4) for the particles in each cell. Next, we begin randomly selecting grid cells to place the new, smaller particles into, with cells of (originally) higher-density selected more frequently. Once a cell is selected, more random-number generation is used to assign values for the new particle's orbital elements based on the calculated statistics for the old cell. Gaussian distributions are used for the eccentricity, inclination, and phase angles while a uniform distribution is used for the X and Y coordinates. The new particle is then added to the output as long as it does not overlap with any other new particles. This process continues until the total mass of new particles matches that of the former set.

As can be seen in Figure 5.2, the redistribution process creates numerous nonphysical vertical lines of alternating high and low density. These "quantization features" are a product of the gaussian distributions used to assign the eccentricity and other orbital elements to new particles. Fortunately, we will see in the next section that they smooth out after just 25-35 orbits.

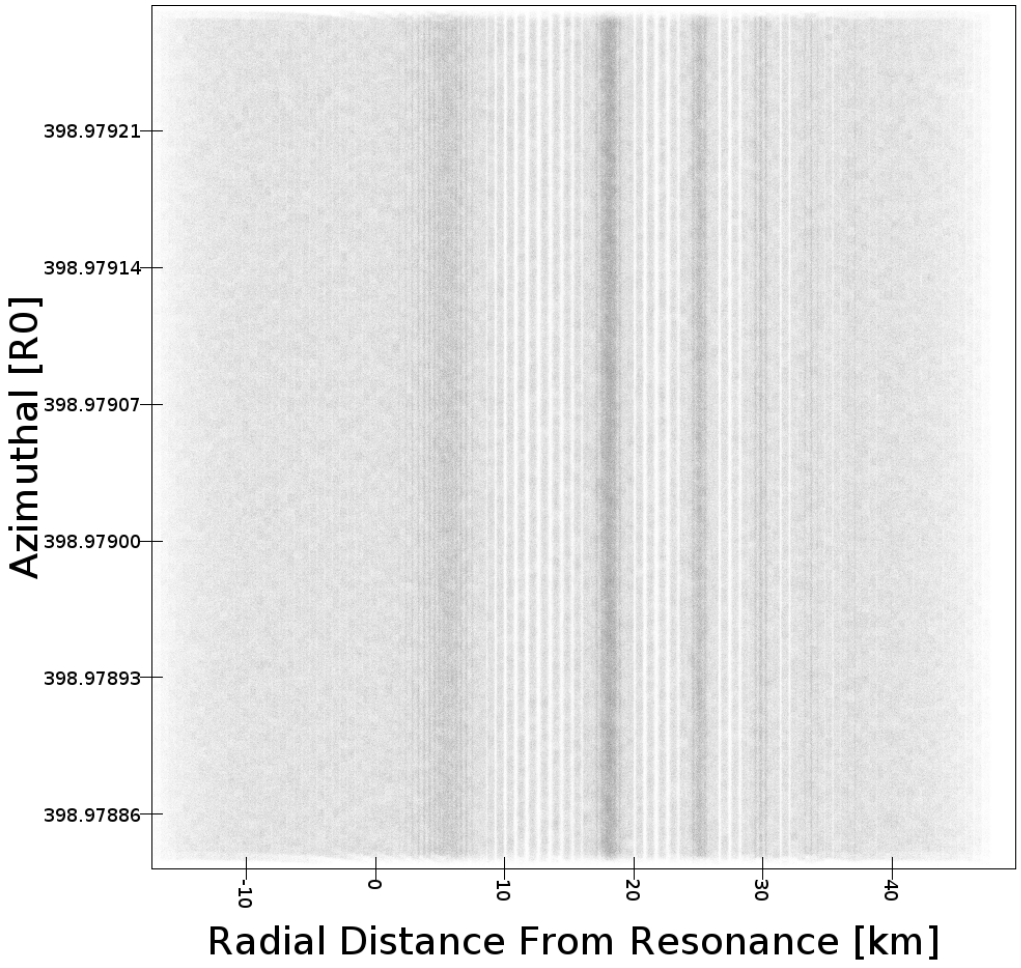

Figure 5.2: A direct plot of particle locations after the initial redistribution. The y-axis is the azimuthal coordinate in units of R_0, the orbital radius of the perturbing moon. The x-axis marks the radial distance from the resonance location.

5.4 Results

We created 2 new ("high" and "super") resolution simulations using the procedure outlined in the preceeding section, the first with about 10.6 million particles (up from 1.3 million) and the second with just over 42.3 million. These correspond to particle sizes (radii) of roughly 4.2m and 2.6m, down from an original 8.4m. Figure 5.3, from 31 orbits into the "super" resolution simulation, shows that the density wave structure is preserved and that

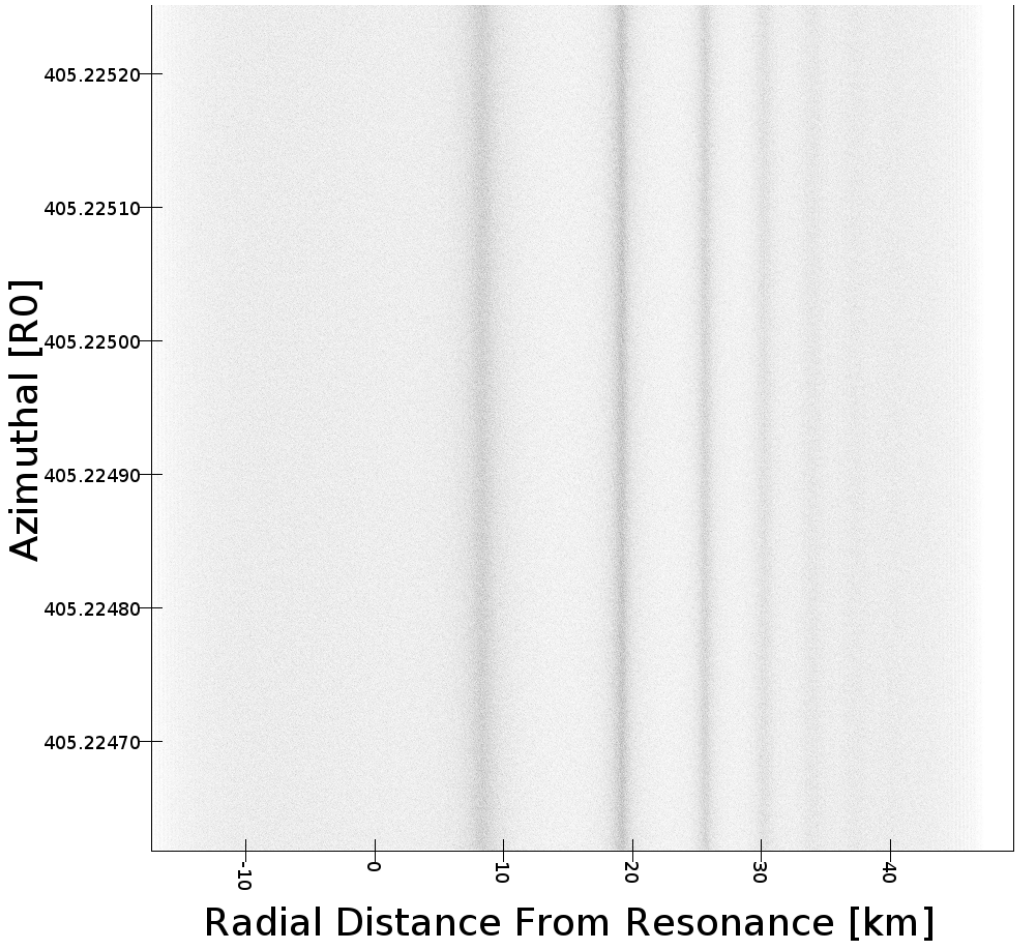

Figure 5.3: A direct plot of the local "super" resolution cell after 31 orbits. (Sub-pixel) black dots represent particles.

quantization features from the redistribution process have smoothed out.

If we zoom in to Figure 5.4, we can compare the finer-grain structure of the highest-amplitude peak of the density wave across the simulations. At left, the original simulation shows significant clumpiness, though it is hard to discern any real patterns. With increased resolution in the plots at center and right, the wave peak is better defined and straw-like clumps clearly form in longer strands on both sides of the peak. In addition, the cant angle changes abruptly from near-perpendicular to near-parallel at the wave peak (moving right

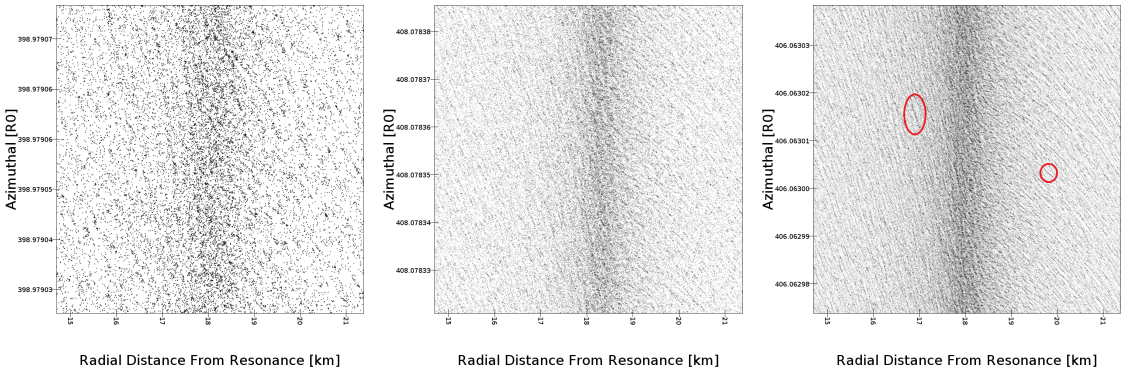

Figure 5.4: Zoom-ins from each of 3 local-cell simulations with increasing resolution from left to right. The area shown is about 1/10 the area of the full cell and is centered on the highest peak of the density wave. At right, red circles highlight two of the many examples of well-resolved straw structure that we are looking for.

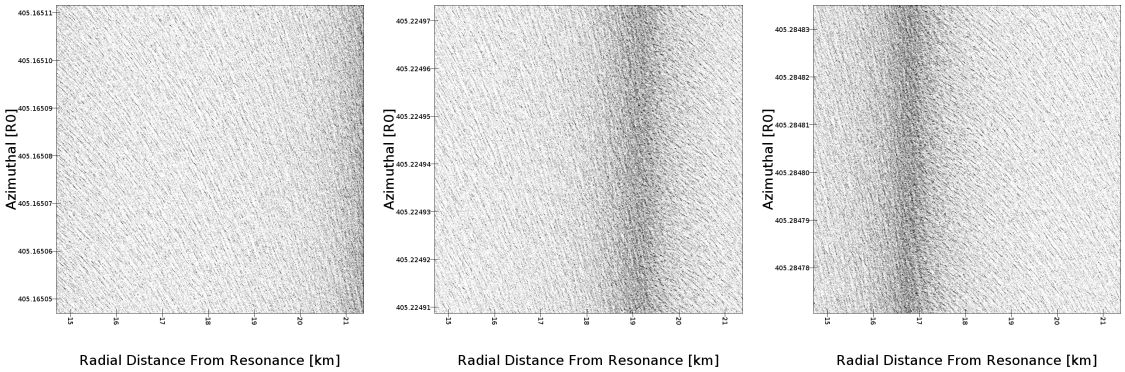

Figure 5.5: Zoom-ins from the super-resolution simulation showing the propagation of the highest wave peak. Individual particles do not move along with the wave but instead oscillate radially about their guiding centers such that collective motion results in a travelling wave. See https://youtu.be/PgtVAHLu_oI for an animated version of this Figure.

to left). These trends are further illuminated by Figure 5.5, which shows the propagation of the highest density wave peak in the "super" resolution simulation.

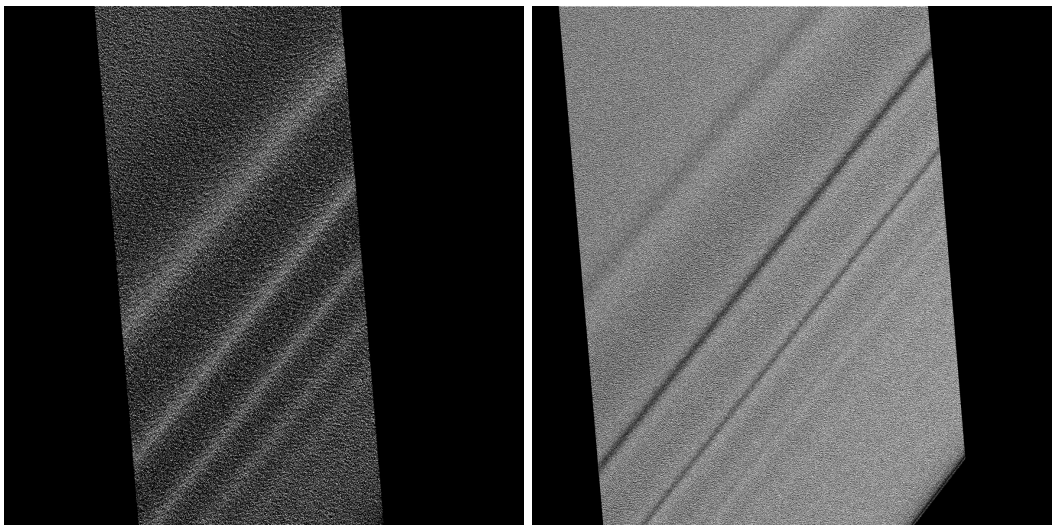

Figure 5.6: Photometric renderings of the original (left) and super (right) resolution simulations. These mimic what an oberver like Cassini might see using optical imaging (Figure 5.1). The ring material is located between the sun and observer for both images.

Figure 5.6 contains the output of a photometric rendering tool [15] applied to the original and super resolution simulations. The renderings approximate the optical view of an observer who looks toward the sun through the ring-plane (from the unlit side). Despite using the same rendering method, the two images are quite distinct, and differ noticeably from direct particle plots (Figures 5.3, 5.4, 5.5). In the lower resolution image, regions between wave peaks appear dark, while the highest-density regions are bright. Due to two competing scattering effects, the opposite is true of the high resolution image, which more closely resembles Figure 5.1. At one extreme, regions of low particle count and surface area provide little opportunity for light to scatter, so photons mostly pass through and the region appears darker. An increase in particle count contributes to increased scattering and therefore brightness. At the opposite extreme, regions of high particle count and surface area provide sufficient material to block the transmission of light, causing the region to

appear dark. A decrease in particle count therefore leads to increased brightness.

Because our method of increasing resolution conserves mass and particle density, it necessarily increases surface area, which is proportional to Nr^2. The relative surface area and optical depth therefore scale linearly with the ratio of the original to final particle radius. Looking again to the photometric renderings of Figure 5.6, this shift (about a factor of 3 here) is clearly enough to push the observed image from one regime of scattering effects to the other. Recalling that the A-ring particle size distribution has an estimated cut-off point around 5m, we may have simply transitioned to a realistic baseline optical depth. The fact that the rendering of the high-resolution simulation qualitatively matches real Cassini images of density waves suggests that our method is valid in capturing the physics of density waves and straw.

Chapter 6

Conclusion

In conclusion, we find that the local cell method is viable and superior to the global cell for the purposes of N-body density wave simulations. Unlike the global cell, which necessitates either impossibly large particle counts or poor resolution for computational feasibility, the local cell is able to capture density wave formation under reasonable run times and resolutions. In accordance with theory and observations, our simulated density waves follow a characteristic decrease in wavelength and amplitude with distance from the resonance location. We also find that simulations with fully formed density waves can be used effectively as initial conditions for new simulations that test perturbations to the standard system. First, sudden removal of the moon was found to result in the damping of the wave over the course of about 1000 orbits, or 1-2 years of real time. The wave did leave behind a region of elevated density just outside the resonance location, an effect which would be interesting to compare against observations of the time-dependent Janus-Epimetheus density waves. Second, increasing the particle count by generating and redistributing an expanded set based on the statistical properties of the original was found to be a useful tactic for improving resolution. Starting a new simulation with the new set as its initial conditions allowed us to "skip" the long density wave formation process and quickly see the higher-resolution straw

features we were interested in. Photometric renderings also confirmed that this process resulted in optically realistic density waves when compared to observation.

Future work would involve the use of our redistribution technique to quickly simulate the formation of other density waves at the minimum possible resolution before enhancing the resolution to observe fine-grain structure. As all simulations considered in this work used a uniform particle-size distribution, it would also be potentially interesting and valuable to apply a power law or other distribution when generating the new particle set. We would also like to repeat the analysis of Section 3.4 on our higher-resolution simulations to examine whether particle size contributes to deviation from the linear theory.

Bibliography

[1] Frank G Bridges, A Hatzes, and DNC Lin. Structure, stability and evolution of saturn's rings. *Nature*, 309(5966):333–335, 1984.

[2] Nikolai Brilliantov, PL Krapivsky, Anna Bodrova, Frank Spahn, Hisao Hayakawa, Vladimir Stadnichuk, and Jürgen Schmidt. Size distribution of particles in saturn's rings from aggregation and fragmentation. *Proceedings of the National Academy of Sciences*, 112(31):9536–9541, 2015.

[3] RG French, W Bridges, M Hedman, P Nicholson, C Mankovich, and C McGhee-French. A panoply of waves in saturn's c ring driven by internal planetary oscillations. In *AAS/Division for Planetary Sciences Meeting Abstracts*, volume 52, pages 513–06, 2020.

[4] William H Julian and Alar Toomre. Non-axisymmetric responses of differentially rotating disks of stars. *The Astrophysical Journal*, 146:810, 1966.

[5] Marius Lehmann, Jürgen Schmidt, and Heikki Salo. Density waves and the viscous overstability in saturn's rings. *Astronomy & Astrophysics*, 623:A121, 2019.

[6] Mark C Lewis and Glen R Stewart. A new methodology for granular flow simulations of planetary rings–coordinates and boundary conditions. In *Proceedings of the IASTED International Conference, Modeling and Simulation*, pages 292–297. ACTA Press, 2002.

[7] Mark C Lewis and Glen R Stewart. Expectations for cassini observations of ring material with nearby moons. *Icarus*, 178(1):124–143, 2005.

[8] Mark C Lewis and GR Stewart. Collisional dynamics of perturbed planetary rings. i. *The Astronomical Journal*, 120(6):3295, 2000.

[9] MC Lewis and GR Stewart. Extended gravity wakes in pan wakes. In *AAS/Division of Dynamical Astronomy Meeting# 36*, pages 09–04, 2005.

[10] JJ Lissauer and JN Cuzzi. Resonances in saturn's rings. *The Astronomical Journal*, 87:1051–1058, 1982.

[11] Carl D Murray and Stanley F Dermott. *Solar system dynamics*. Cambridge university press, 1999.

[12] Carolyn C Porco, PC Thomas, JW Weiss, and DC Richardson. Saturn's small inner satellites: Clues to their origins. *science*, 318(5856):1602–1607, 2007.

[13] CC Porco, E Baker, J Barbara, K Beurle, A Brahic, JA Burns, S Charnoz, N Cooper, DD Dawson, AD Del Genio, et al. Cassini imaging science: Initial results on saturn's rings and small satellites. *science*, 307(5713):1226–1236, 2005.

[14] Morgan E Rehnberg, Larry W Esposito, Zarah L Brown, Nicole Albers, Miodrag Sremčević, and Glen R Stewart. A traveling feature in saturn's rings. *Icarus*, 279:100–108, 2016.

[15] Elizabeth Ruetschle, Lance Ellis, and Mark C. Lewis. Photometric rendering of dust and freed regolith in ring simulations. In *19th International Conference on Scientific Computing*, 2021.

[16] Frank H Shu. Waves in planetary rings. In *IAU Colloq. 75: Planetary Rings*, pages 513–561, 1984.

[17] Linda J Spilker, Stuart Pilorz, Arthur L Lane, Robert M Nelson, Benjamin Pollard, and Christopher T Russell. Saturn a ring surface mass densities from spiral density wave dispersion behavior. *Icarus*, 171(2):372–390, 2004.

[18] Glen R Stewart. Nonlinear satellite wakes in planetary rings: I. phase-space kinematics. *Icarus*, 94(2):436–450, 1991.

[19] Matthew S Tiscareno, Philip D Nicholson, Jeffrey N Cuzzi, Linda J Spilker, Carl D Murray, Matthew M Hedman, Joshua E Colwell, Joseph A Burns, Shawn M Brooks, Roger N Clark, et al. Close-range remote sensing of saturn's rings during cassini's ring-grazing orbits and grand finale. *Science*, 364(6445), 2019.